# Multiregion Light Control in Diffusive Media via Wavefront Shaping

Liam Shaughnessy,[1,†] Rohin E. McIntosh,[1,†] Arthur Goetschy,[2] Chia Wei Hsu,[3] Nicholas Bender,[4] Hasan Yılmaz,[5] Alexey Yamilov,[6] and Hui Cao[1,*]

[1]Department of Applied Physics, Yale University, New Haven, Connecticut 06520, USA
[2]Institut Langevin, ESPCI Paris, PSL University, CNRS, F-75005 Paris, France
[3]Ming Hsieh Department of Electrical and Computer Engineering, University of Southern California, Los Angeles, California 90089, USA
[4]School of Applied and Engineering Physics, Cornell University, Ithaca, New York 14850, USA
[5]Institute of Materials Science and Nanotechnology, National Nanotechnology Research Center (UNAM), Bilkent University, 06800 Ankara, Turkey
[6]Physics Department, Missouri University of Science & Technology, Rolla, Missouri, USA

(Received 5 August 2023; accepted 1 July 2024; published 2 October 2024)

Wavefront shaping allows focusing light through or inside strongly scattering media, but the background intensity also increases which reduces the target's contrast. By combining transmission or deposition matrices for different regions, we construct joint operators to achieve spatially resolved control of light in diffusive systems. The eigenmode of a contrast operator can maximize the power contrast between a target and its surrounding. A difference operator enhances the power delivery to a target while avoiding the background increase. This work opens the door to coherent control of nonlocal effects in wave transport for practical applications.

DOI: 10.1103/PhysRevLett.133.146901

Nonlocal correlations between multiply scattered waves are a hallmark of mesoscopic transport in diffusive systems [1–12]. Long-range spatial correlations have direct consequences for controlling mesoscopic transport with wavefront shaping [13–15]. Positive intensity correlations facilitate the total transmission enhancement and power delivery to an extended target by optimizing a single incident wavefront [16–21]. Such correlations also increase the background intensity, thus limiting the target-to-background contrast [22–27].

For practical applications including optical communication, photothermal therapy, microsurgery, and optogenetics [28–32], it is important not only to maximize light intensity on a target but also to optimize the target-to-background intensity contrast. Enhancing the contrast requires suppressing positive intensity correlations between the target and background or, even better, introducing negative correlations between their intensity changes. This is challenging to realize, given the constraints of nonlocal correlations. Our aim of this work is to utilize long-range correlations for power delivery to an extended target and simultaneously overcome positive correlations to maximize the target-to-background contrast.

For this goal, we introduce two operators: the contrast operator and the difference operator. We demonstrate that the contrast operator's eigenvectors can maximize the target-to-background intensity contrast. Strong intensity attenuation in a chosen surrounding area enables the generation of high-contrast patterns behind the scattering medium by shaping the incident wavefront of a coherent beam (Fig. 1). However, the slight intensity increase on the target may not be optimal for applications. To enhance the target intensity as much as possible with little change in the surrounding intensity, we introduce the difference operator. Its eigenvectors are used for broad-area focusing behind a thick scattering sample and for targeted power delivery deep inside a diffusive waveguide. We identify and theoretically justify a robust scaling between intensity changes in the target and background, which explains the superior performance of

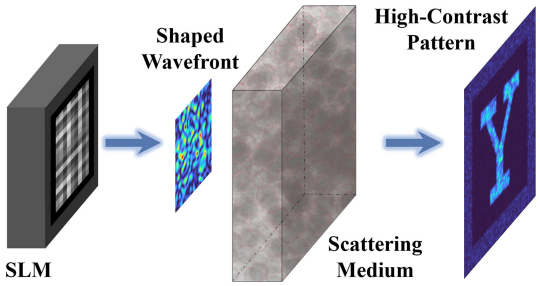


FIG. 1. Schematic for the propagation of an eigenstate of the contrast operator. A high-contrast pattern with a sharp boundary is created behind a disordered slab by shaping the incident wavefront of a laser beam with a spatial light modulator. The high-contrast pattern of the letter Y is generated with an experimentally measured transmission matrix.

[†]These authors contributed equally to this work.
[*]Contact author: hui.cao@yale.edu

 

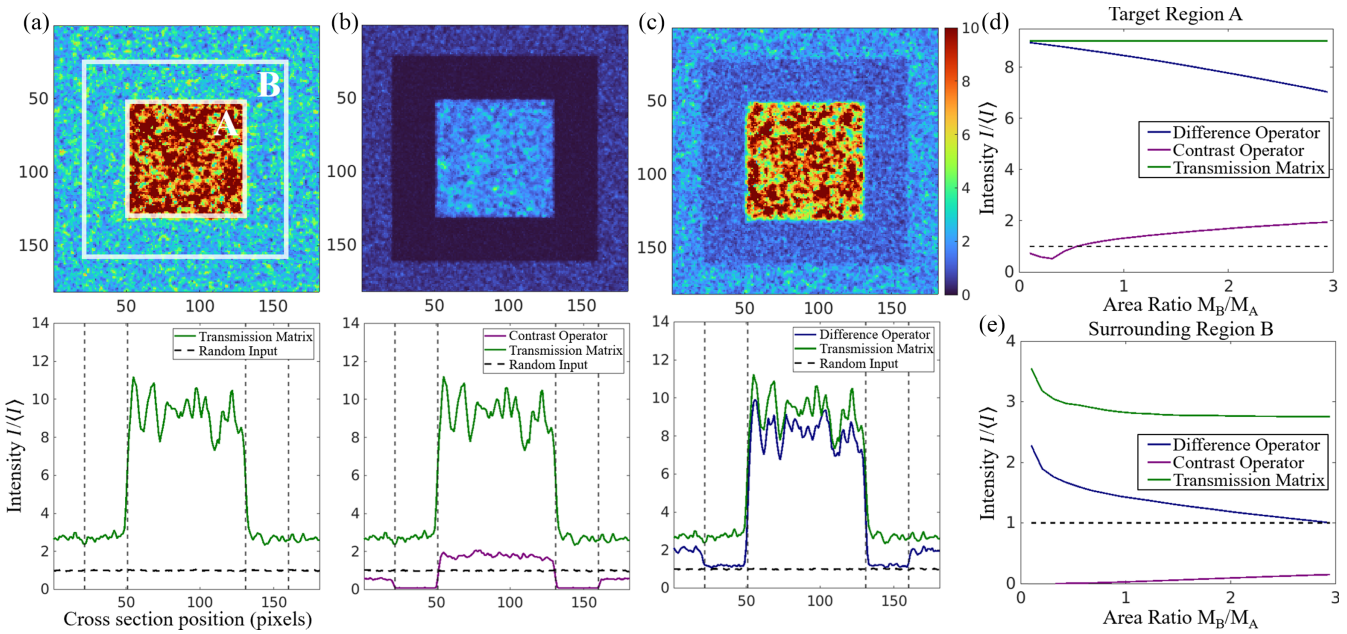


FIG. 2. Eigenstates of transmission, contrast, and difference operators. Spatial distributions of transmitted intensity $I$ through a multiple-scattering slab for eigenstates with maximal power inside the target region $A$ (a), highest contrast of power in $A$ to that in a surrounding region $B$ (b), largest power difference between $A$ and $B$ (c). All intensities are normalized by the mean intensity $\langle I\rangle$ with random illuminations, and averaged over the ten eigenvectors with largest eigenvalues. Lower panels show intensity across a cross section of the images in the upper panels. The green curve represents the state in (a), purple in (b), blue in (c), and black dashed line for random input wavefront. The square $A$ is 907 μm × 907 μm, and ring $B$ has an outer dimension of 1580 μm (with twice the area as $A$). One camera pixel (px) has a lateral size of 5.6 μm. Enhancement of mean intensity in target $A$ (d), surrounding region $B$ (e) over that under random illuminations, as a function of the area ratio given by the ratio of the number of speckles $M_B/M_A$. The contrast eigenstate (magenta) has an intensity increase in $A$ and $B$ with $M_B/M_A$ ratio, while the difference eigenstate (blue) has an intensity decrease in both regions. The black dashed line corresponds to random input wavefront.

the difference operator. Experimentally, we demonstrate a tenfold difference in the relative intensity change between background and target regions with the same area.

We first investigate the focusing of light onto an extended area behind a three-dimensional (3D) scattering slab. The sample consists of ZnO nanoparticles that are spin coated on a cover slide. The ZnO layer thickness is measured to be 60 μm. The transmittance at normal incidence at the probe wavelength of $\lambda = 532$ nm is measured to be 0.03, which yields a transport mean free path ∼1 μm [33]. As schematically shown in Fig. 1, the incident wavefront of a monochromatic laser beam is modulated by a phase-only spatial light modulator (SLM) before illuminating the ZnO slab. The illumination spot on the sample surface has a 24 μm diameter. The number of input spatial channels modulated by the SLM is $M_1 = 2048$ for two orthogonal polarizations. A CCD camera is placed at the Fourier plane of the output surface of the slab to measure the transmitted intensity patterns. Using a phase-stepping common-path interferometric method, we measure the (partial) transmission matrix [17,20,34]. More details are given in Sec. I of the Supplemental Material [35].

In Fig. 2(a), the target region (labeled as "$A$") is a square at the center of the field of view on the CCD camera, containing $M_A \simeq 876$ speckle grains. The matrix $t_A$ maps the incident fields to the transmitted fields inside area $A$. The eigenvector of $t_A^\dagger t_A$ with the largest eigenvalue gives the optimal incident wavefront for focusing transmitted light to target $A$ [20]. While the mean intensity within $A$, $I_A$, is almost 10 times larger than the intensity $\langle I\rangle$ under random wavefront illumination, the intensity outside $A$, $I_B$, is more than doubled. The target intensity enhancement, predicted by the theoretical model in Ref. [20], is $I_A/\langle I\rangle \simeq 9.1$ (see Supplemental Material, Sec. II for details) [35]. Such large enhancement is a result of nonlocal intensity correlations between different speckles inside $A$, as revealed by the approximate expression $I_A/\langle I\rangle \simeq (1+\sqrt{M_1/M_A + M_1 C_2})^2$. Here $C_2$ denotes the weight of nonlocal correlations that can be computed explicitly from the characteristics of the disordered sample and illumination condition. As detailed in Supplemental Material, Sec. II [35], we can also estimate the intensity increase outside the target region. For a moderate extent of the target $A$, the background intensity enhancement is $I_B/\langle I\rangle \simeq 1 + M_1 C_2$. This gives $I_B/\langle I\rangle \simeq 1.9$, which agrees with our experimental data for $M_A \lesssim 200$ (Supplemental Material, Fig. S1), but it slightly underestimates the actual value for the large target in Fig. 2(a).

To suppress the intensity increase in a surrounding area [labeled $B$ in Fig. 2(a)], we introduce the contrast operator $(t_B^\dagger t_B)^{-1} t_A^\dagger t_A$, where $t_B$ denotes the matrix that maps incident fields to transmitted fields in $B$ (see Supplemental Material, Sec. III [35] for details). Figure 2 shows an example with the area ratio of $B$ to $A$, $M_B/M_A$, equal to 2. As shown in Fig. 2(b), the intensity in $B$ nearly vanishes, while the intensity in $A$ is slightly above the value for random wavefront illumination. Such changes are caused by strong destructive interference of scattered waves in $B$ and weak constructive interference in $A$.

There is a sharp transition between $A$ and $B$: the intensity changes abruptly across the boundary of $A$ and $B$. The opposite changes of intensity in $A$ and $B$ are surprising because of the widely known positive intensity correlations of multiply scattered light. This is a result of the wave interference effect. Hence, the spatial intensity correlations can be overcome by manipulating interference effects with wavefront shaping.

The maximal target-to-background contrast in Fig. 2(b) is achieved mostly by suppressing the background intensity instead of enhancing the target intensity. Some applications like photodynamic therapy and microsurgery benefit more from intensity enhancement of the target than suppression of background intensity. To keep the background intensity nearly unchanged from that with random wavefront illumination while increasing the target intensity as much as possible, we introduce the difference operator $t_A^\dagger t_A - t_B^\dagger t_B$. Its maximal eigenvalue is the largest possible difference in transmission between area $A$ and $B$, and the corresponding eigenvector gives the incident wavefront. Figure 2(c) shows the target intensity is reduced slightly from focusing to $A$; meanwhile, the surrounding intensity barely deviates from that with random wavefront illumination.

With the target region $A$ being fixed, we vary the surrounding area $B$ and compare the contrast eigenstates to the difference eigenstates. As the area ratio $M_B/M_A$ of $B$ over $A$ increases, the highest-contrast state features intensity growth in both $A$ and $B$ [Figs. 2(d) and 2(e)]. The attenuation of surrounding intensity becomes less efficient for larger $B$, leading to lower target-to-background contrast. The largest-difference state exhibits an opposite behavior: intensity decreases in both regions with increasing $M_B/M_A$ [Figs. 2(d) and 2(e)]. At a small $M_B/M_A$ ratio, the power difference between $A$ and $B$ is maximized mostly by enhancing the target intensity because $A$ dominates over $B$. For a large $M_B/M_A$ ratio, the maximal power difference is achieved by avoiding the increase of background intensity, as $B$ becomes dominant over $A$.

We analyze the transmission drops $\Delta T_A$ and $\Delta T_B$, in $A$ and $B$, respectively, of the largest-difference eigenstate from the state with maximum power in $A$, for various values of $M_A$ and $M_B$. As shown in the inset of Fig. 3, $\Delta T_B$ scales linearly with $\Delta T_A$: $\Delta T_B \simeq \alpha \Delta T_A$, with $\alpha = 2.5$.

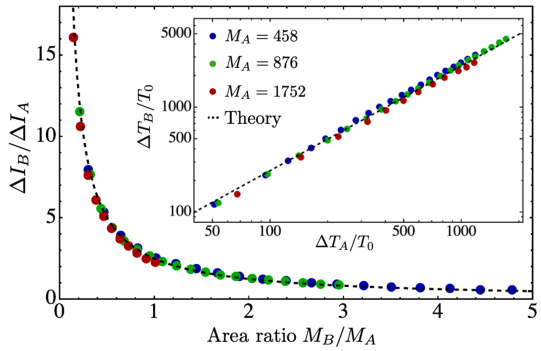


FIG. 3. Scaling analysis for largest-difference eigenstate. Transmission reduction $\Delta T$ and intensity drop $\Delta I$ in target region $A$ and surrounding area $B$ for the largest eigenstate of $t_A^\dagger t_A - t_B^\dagger t_B$ from that of $t_A^\dagger t_A$ for varying sizes $M_A$ and $M_B$ (different data points with the same color correspond to different $M_B$). All points collapse to a single curve when the relative variations $\Delta I_B/\Delta I_A$ are plotted as a function of $M_B/M_A$. The inset shows the linear scaling of the power drops in $A$ and $B$; both are normalized by the transmission of a single speckle grain $T_0$ for random input wavefront. Theoretical prediction $\Delta T_B = \alpha \Delta T_A$ (dashed line) agrees well with the experimental data (dots) for $\alpha = 2.5$.

Such scaling results in the intensity variation $\Delta I_B \simeq \alpha (M_A/M_B) \Delta I_A$ in Fig. 3. This relation explicitly shows that intensity drop in $B$ can be much greater than that in $A$, allowing us to maximize target-to-background difference while preserving high power in $A$. For example, with $M_A \simeq 876$ as in Fig. 2, $I_A/I_B \simeq 4$ for the state with maximum power in $A$, and the intensity drop of the largest-difference eigenstate is $\Delta I_B/I_B \simeq 10 \Delta I_A/I_A$ for $M_B = M_A$. The above scaling can be predicted theoretically by treating $t_B^\dagger t_B$ as a perturbation of $t_A^\dagger t_A$ (Supplemental Material, Sec. IV A–C) [35]. Second-order perturbation theory gives $\alpha = 2$, while including the third-order perturbation further increases $\alpha$. Experimentally, this scaling holds for $M_B/M_A$ up to 5. Using the perturbative approach, we are also able to link the quick drop of $I_B$ in Fig. 2(e) to nonlocal correlation and to explain the observed linear decrease in $I_A$ with the area ratio $M_B/M_A$ in Fig. 2(d) (Supplemental Material, Sec. IV C and Fig. 2) [35].

In addition to controlling power in transmission, targeted power delivery deep into a multiple-scattering system has important applications. We show next that the difference operator is also useful for delivering power to an extended target deep inside a two-dimensional (2D) diffusive waveguide by incident wavefront shaping. The planar waveguide structure is fabricated in a silicon-on-insulator wafer by electron beam lithography and reactive plasma etching [18,36]. As shown in Fig. 4(a), 100 nm diameter holes are randomly distributed in the waveguide, which has photonic crystal sidewalls to reflect light. The waveguide is 15 μm wide, supporting $M_1 = 55$ propagating modes at the probe wavelength $\lambda = 1.55$ μm. The transport mean free path $\ell_t = 3.2$ μm is much shorter than the disordered

region length $L = 50$ μm in the waveguide [37]. Hence, incident light from one end of the waveguide undergoes multiple scattering and diffusive transport through the waveguide. A small amount of light scatters out-of-plane from the air holes, providing a direct probe of field distribution inside the disordered region. While the material absorption is negligible, the out-of-plane scattering can be modeled as an effective loss and accounted for in the diffusive dissipation length $\xi_a = 28$ μm [18].

Using an SLM, we shape the one-dimensional (1D) incident wavefront of a continuous-wave laser beam at $\lambda = 1.55$ μm before launching the light through the edge of the wafer into a ridge waveguide that is connected to the disordered waveguide. The out-of-plane scattered light overlaps with a flat-phase-front reference beam, and a camera records their interference pattern. From the image, the internal field distribution is reconstructed with a spatial resolution of 1.1 μm.

In Fig. 4, we choose the target region $A$ to be a 10 μm × 10 μm square centered at depth $z_D = 40$ μm. From the interferometric measurement, we retrieve the scattered field everywhere inside the disordered waveguide and construct the deposition matrix $\mathcal{Z}_A$ that maps the incident wavefront to the field distribution within the target region [21]. The largest eigenvalue of $\mathcal{Z}_A^\dagger \mathcal{Z}_A$ gives the maximal possible power (spatially integrated intensity) that can be delivered to the target area $A$. As shown in Ref. [21], for a target of size much larger than the wavelength, the maximum-deposition eigenstate has an approximate scaling of the target intensity enhancement as $I_A/\langle I\rangle \simeq 3M_1C_2/2$. In a diffusive waveguide, the long-range correlation $C_2$ has a very different expression from that of an open slab [17], and gives a large enhancement, e.g., $I_A/\langle I\rangle \simeq 15$ at $z_D = 40$ μm, when controlling all input channels [21]. However, the intensity outside $A$ is notably higher than that under random wavefront illumination, as shown by the green curve in Fig. 4. On one hand, long-range correlation allows a single input wavefront to enhance intensity everywhere within $A$. On the other hand, it also causes an intensity increase outside $A$.

To suppress the intensity enhancement right before $A$, we select region $B$ as a 10 μm × 10 μm square centered at depth $z_D = 30$ μm, as illustrated in Fig. 4(a). The deposition matrix from input field to region $B$ is $\mathcal{Z}_B$. To prevent the intensity in $B$ from increasing with that in $A$, we use the difference operator $\mathcal{Z}_A^\dagger \mathcal{Z}_A - \mathcal{Z}_B^\dagger \mathcal{Z}_B$. Its eigenstate with maximal eigenvalue keeps the intensity in $B$ almost equal to the value of random inputs while dramatically raising the intensity in $A$ [blue curve in Fig. 4(b)]. We further increase the length of region $B$ and modify the difference operator $\mathcal{D} = \mathcal{Z}_A^\dagger \mathcal{Z}_A - \gamma \mathcal{Z}_B^\dagger \mathcal{Z}_B$, where $\gamma = M_A/M_B$ is equal to the area ratio of $A$ to $B$. Incorporating $\gamma$ to the difference operator would reduce the contribution from $B$ when its area exceeds $A$ so that the maximal difference between $A$ and $B$ is achieved by enhancing power in $A$ ($U_A$) more than by suppressing power in $B$ ($U_B$). In Figs. 4(c) and 4(d), the maximal difference eigenstates, for area $B$ equal to twice and even 3 times area $A$, feature significant intensity enhancement in $A$ while the intensity in $B$ barely increases.

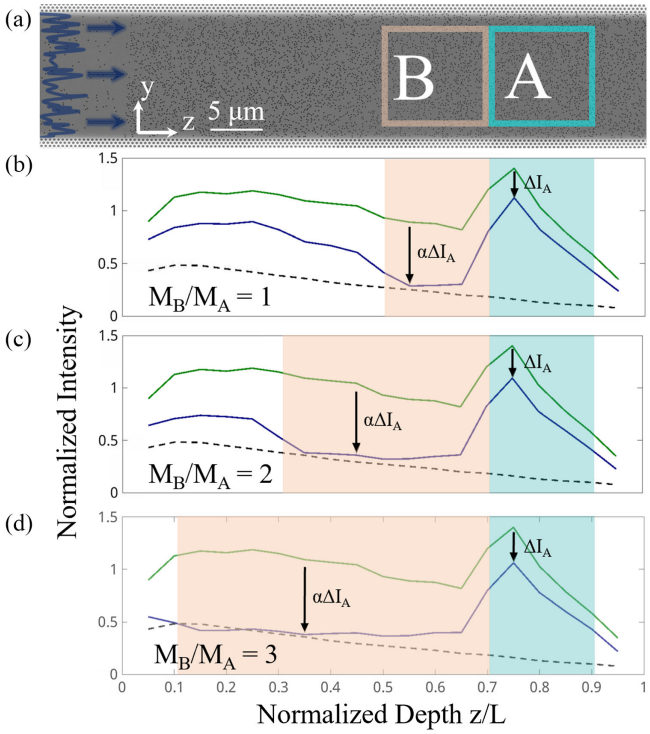


FIG. 4. Difference eigenstate for targeted power delivery into a diffusive waveguide. (a) Scanning electron microscopy image of the disordered waveguide. Shaping the wavefronts of incident light into a disordered waveguide enhances the power within an extended target $A$ (shaded cyan) while minimizing the intensity increase in region $B$ (shaded almond) right in front of $A$. The silicon waveguide has a random array of air holes over a region of length 50 μm and width 15 μm. Target $A$ is a 10 × 10 μm$^2$ square centered at depth 40 μm. Region $B$ is 10 μm wide and its length varies from 10 to 30 μm. (b)–(d) Cross-section averaged intensities for $M_B/M_A$ equal to 1 (b), 2 (c), 3 (d). The deposition eigenstates (green) increase intensities in both $A$ and $B$, while the difference eigenstates (blue) enhance intensity in $A$ with little change of intensity in $B$ from random input wavefronts (black dashed). The intensity is normalized by $\langle I_A\rangle$, the average intensity in target $A$ by the maximum deposition eigenstate. The arrows indicate the average intensity difference between the deposition and difference eigenstates in the region $A$, $\Delta I_A$, and region $B$, $\Delta I_B \simeq \alpha \Delta I_A$ for $\alpha = 2.2$.

Comparing the maximal difference eigenstate to the maximal deposition eigenstate, we find that the power reduction in $B$ ($U_B$) is notably larger than that in $A$ ($U_A$). The largest eigenvalue of $\mathcal{D}$ maximizes $U_A - \gamma U_B$, while the maximal eigenvalue of $\mathcal{Z}_A^\dagger \mathcal{Z}_A$ gives the highest possible $U_A$. Since it is impossible to increase $U_A$ beyond the maximal deposition eigenvalue, the only way to enhance the difference between $U_A$ and $U_B$ is to reduce $U_B$ much more than $U_A$ for the largest-difference state.

Thus, the background intensity increase, seen in the maximal-deposition eigenstate, is suppressed in the largest-difference state.

A quantitative explanation is obtained by generalizing the perturbative approach developed for transmission. We show in Supplemental Material, Sec. II D [35] that the largest eigenvalue of $\mathcal{D}$, as well as the powers $U_A$ and $U_B$ deposited in $A$ and $B$ by the corresponding eigenstate, can be quantitatively predicted from the knowledge of the eigenstates and eigenvalues of $\mathcal{Z}_A^\dagger \mathcal{Z}_A$ only, using third-order perturbation theory (Supplemental Material [35], Fig. S3). The mean intensity reductions in $B$ and $A$ are related by $\Delta I_B \simeq (\alpha/\gamma)(M_A/M_B)\Delta I_A$, with $\alpha = 2$ using second-order perturbation and $\alpha > 2$ including third-order perturbation. Hence, by choosing $\gamma = M_A/M_B$, the background intensity drop $\Delta I_B$ remains constant for varying areas of $B$, and the drop power $\Delta U_B$ increases linearly with $B$ area, as shown in Fig. 4. We thus combine the advantages of a much greater relative intensity change in the background than in the target ($\Delta I_B/I_B \gg \Delta I_A/I_A$) and a large background domain over which the intensity difference from the target is maximized.

In conclusion, we introduce the contrast operator to reach the highest possible contrast and the difference operator to realize the largest possible power difference between target and background. However, it is impossible to simultaneously achieve the maximum contrast and the maximum difference, because the corresponding optimal eigenstates do not coincide. Nevertheless, it is possible to increase both contrast and difference, e.g., using the regularized contrast operator as shown in the Supplemental Material [35] (Sec. V, Fig. S4). The trade-off between the target enhancement and the target-to-background contrast can be adjusted for specific applications.

*Acknowledgments*—This work is supported partly by the US National Science Foundation (NSF) under Grants No. DMR-1905465, No. DMR-1905442 and No. ECCS-2146021, and by the US Office of Naval Research (ONR) under Grant No. N00014-221-1-2026 and by the French Government under the program Investissements d'Avenir.

[1] N. Garcia and A. Z. Genack, Crossover to strong intensity correlation for microwave radiation in random media, Phys. Rev. Lett. **63**, 1678 (1989).

[2] M. P. van Albada, J. F. de Boer, and A. Lagendijk, Observation of long-range intensity correlation in the transport of coherent light through a random medium, Phys. Rev. Lett. **64**, 2787 (1990).

[3] A. Z. Genack, N. Garcia, and W. Polkosnik, Long-range intensity correlation in random media, Phys. Rev. Lett. **65**, 2129 (1990).

[4] J. F. de Boer, M. P. van Albada, and A. Lagendijk, Transmission and intensity correlations in wave propagation through random media, Phys. Rev. B **45**, 658 (1992).

[5] R. Berkovits and S. Feng, Correlations in coherent multiple scattering, Phys. Rep. **238**, 135 (1994).

[6] F. Scheffold and G. Maret, Universal conductance fluctuations of light, Phys. Rev. Lett. **81**, 5800 (1998).

[7] M. C. W. van Rossum and T. M. Nieuwenhuizen, Multiple scattering of classical waves: Microscopy, mesoscopy, and diffusion, Rev. Mod. Phys. **71**, 313 (1999).

[8] P. Sebbah, R. Pnini, and A. Z. Genack, Field and intensity correlation in random media, Phys. Rev. E **62**, 7348 (2000).

[9] P. Sebbah, B. Hu, A. Z. Genack, R. Pnini, and B. Shapiro, Spatial-field correlation: The building block of mesoscopic fluctuations, Phys. Rev. Lett. **88**, 123901 (2002).

[10] T. Strudley, T. Zehender, C. Blejean, E. P. A. M. Bakkers, and O. L. Muskens, Mesoscopic light transport by very strong collective multiple scattering in nanowire mats, Nat. Photonics **7**, 413 (2013).

[11] R. Sarma, A. Yamilov, P. Neupane, and H. Cao, Using geometry to manipulate long-range correlation of light inside disordered media, Phys. Rev. B **92**, 180203(R) (2015).

[12] I. Starshynov, A. M. Paniagua-Diaz, N. Fayard, A. Goetschy, R. Pierrat, R. Carminati, and J. Bertolotti, Non-Gaussian correlations between reflected and transmitted intensity patterns emerging from opaque disordered media, Phys. Rev. X **8**, 021041 (2018).

[13] A. P. Mosk, A. Lagendijk, G. Lerosey, and M. Fink, Controlling waves in space and time for imaging and focusing in complex media, Nat. Photonics **6**, 283 (2012).

[14] S. Rotter and S. Gigan, Light fields in complex media: Mesoscopic scattering meets wave control, Rev. Mod. Phys. **89**, 015005 (2017).

[15] H. Cao, A. P. Mosk, and S. Rotter, Shaping the propagation of light in complex media, Nat. Phys. **18**, 994 (2022).

[16] S. Popoff, G. Lerosey, M. Fink, A. C. Boccara, and S. Gigan, Image transmission through an opaque material, Nat. Commun. **1**, 81 (2010).

[17] S. M. Popoff, A. Goetschy, S. F. Liew, A. D. Stone, and H. Cao, Coherent control of total transmission of light through disordered media, Phys. Rev. Lett. **112**, 133903 (2014).

[18] R. Sarma, A. G. Yamilov, S. Petrenko, Y. Bromberg, and H. Cao, Control of energy density inside a disordered medium by coupling to open or closed channels, Phys. Rev. Lett. **117**, 086803 (2016).

[19] C. W. Hsu, A. Goetschy, Y. Bromberg, A. D. Stone, and H. Cao, Broadband coherent enhancement of transmission and absorption in disordered media, Phys. Rev. Lett. **115**, 223901 (2015).

[20] C. W. Hsu, S. F. Liew, A. Goetschy, H. Cao, and A. Douglas Stone, Correlation-enhanced control of wave focusing in disordered media, Nat. Phys. **13**, 497 (2017).

[21] N. Bender, A. Yamilov, A. Goetschy, H. Yılmaz, C. W. Hsu, and H. Cao, Depth-targeted energy delivery deep inside scattering media, Nat. Phys. **18**, 309 (2022).

[22] I. M. Vellekoop and A. Mosk, Focusing coherent light through opaque strongly scattering media, Opt. Lett. **32**, 2309 (2007).

[23] Z. Yaqoob, D. Psaltis, M. S. Feld, and C. Yang, Optical phase conjugation for turbidity suppression in biological samples, Nat. Photonics **2**, 110 (2008).
[24] I. M. Vellekoop and A. P. Mosk, Universal optimal transmission of light through disordered materials, Phys. Rev. Lett. **101**, 120601 (2008).
[25] S. M. Popoff, G. Lerosey, R. Carminati, M. Fink, A. C. Boccara, and S. Gigan, Measuring the transmission matrix in optics: An approach to the study and control of light propagation in disordered media, Phys. Rev. Lett. **104** (2010).
[26] M. Davy, Z. Shi, and A. Z. Genack, Focusing through random media: Eigenchannel participation number and intensity correlation, Phys. Rev. B **85**, 035105 (2012).
[27] X. Cheng and A. Z. Genack, Focusing and energy deposition inside random media, Opt. Lett. **39**, 6324 (2014).
[28] M. F. Yanik, H. Cinar, H. N. Cinar, A. D. Chisholm, Y. Jin, and A. Ben-Yakar, Neurosurgery: Functional regeneration after laser axotomy, Nature (London) **432**, 822 (2004).
[29] L. Fenno, O. Yizhar, and K. Deisseroth, The development and application of optogenetics, Annu. Rev. Neurosci. **34**, 389 (2011).
[30] H. Yu, J. Park, K. Lee, J. Yoon, K. Kim, S. Lee, and Y. Park, Recent advances in wavefront shaping techniques for biomedical applications, Curr. Appl. Phys. **15**, 632 (2015).
[31] H. Ruan, J. Brake, J. E. Robinson, Y. Liu, M. Jang, C. Xiao, C. Zhou, V. Gradinaru, and C. Yang, Deep tissue optical focusing and optogenetic modulation with time-reversed ultrasonically encoded light, Sci. Adv. **3**, eaao5520 (2017).
[32] N. C. Pégard, A. R. Mardinly, I. A. Oldenburg, S. Sridharan, L. Waller, and H. Adesnik, Three-dimensional scanless holographic optogenetics with temporal focusing (3D-shot), Nat. Commun. **8**, 1228 (2017).
[33] E. Akkermans and G. Montambaux, *Mesoscopic Physics of Electrons and Photons* (Cambridge University Press, Cambridge, England, 2007).
[34] H. Yılmaz, C. W. Hsu, A. Yamilov, and H. Cao, Transverse localization of transmission eigenchannels, Nat. Photonics **13**, 352 (2019).
[35] See Supplemental Material at http://link.aps.org/supplemental/10.1103/PhysRevLett.133.146901 for details of the experimental setup, theory of transmission and contrast operators, perturbative approach, and regularization of the contrast operator.
[36] N. Bender, A. Yamilov, H. Yılmaz, and H. Cao, Fluctuations and correlations of transmission eigenchannels in diffusive media, Phys. Rev. Lett. **125**, 165901 (2020).
[37] A. G. Yamilov, R. Sarma, B. Redding, B. Payne, H. Noh, and H. Cao, Position-dependent diffusion of light in disordered waveguides, Phys. Rev. Lett. **112**, 023904 (2014).